

Testing Hydrodynamic Models of LMC X-4 with UV and X-ray Spectra

Bram Boroson and Timothy Kallman

Goddard Space Flight Center, Greenbelt, MD 20771; bboroson@falafel.gsfc.nasa.gov,
tim@xstar.gsfc.nasa.gov

and

John M. Blondin and Michael P. Owen

Department of Physics, North Carolina State University; blondin@tigger.physics.ncsu.edu,
owen@anubis.physics.ncsu.edu

ABSTRACT

We compare the predictions of hydrodynamic models of the LMC X-4 X-ray binary system with observations of UV P Cygni lines with the GHRS and STIS spectrographs on the Hubble Space Telescope. The hydrodynamic model determines density and velocity fields of the stellar wind, wind-compressed disk, accretion stream, Keplerian accretion disk, and accretion disk wind. We use a Monte Carlo code to determine the UV P Cygni line profiles by simulating the radiative transfer of UV photons that originate on the star and are scattered in the wind. The qualitative orbital variation predicted is similar to that observed, although the model fails to reproduce the strong orbital asymmetry (the observed absorption is strongest for $\phi > 0.5$). The model predicts a mid-eclipse X-ray spectrum, due almost entirely to Compton scattering, with a factor 4 less flux than observed with ASCA. We discuss how the model may need to be altered to explain the spectral variability of the system.

1. Introduction

The mass transfer in High Mass X-ray binaries (HMXB) has proved to be difficult to understand in spite of the simplicity of the first analytic descriptions of accretion from a wind (Bondi & Hoyle 1944). Problems arise in the theory, for example, when X-ray feedback on the dynamics is considered (MacGregor & Vitello 1982; Ho & Arons 1987). The feedback between the X-ray source and a stellar wind can be severe, as the mass accretion rate of a stellar wind depends on $v_w^{-1}v_{\text{rel}}^{-3} = v_w^{-1}(v_w^2 + v_x^2)^{-3/2}$, where v_{rel} is the velocity of an

X-ray source with orbital velocity v_x relative to a stellar wind with velocity v_w . The X-rays can reduce v_w by ionizing to higher stages those ions responsible for the acceleration of the wind.

Even isolated stellar winds are complex. The line-scattering force accelerating the wind depends on the wind velocity gradient. This leads to instabilities such as shocks (MacGregor, Hartmann, & Raymond 1979; Abbott 1980; Lucy & White 1980; Owocki & Rybicki 1984) and nonlinearities which are difficult to model numerically (Owocki, Castor, & Rybicki 1988).

Near orbital phase $\phi = 0.8$ many X-ray binaries show “pre-eclipse dips” that may be caused when the gas stream that feeds the disk passes over the line of sight. Even systems such as 4U 1700-377 thought to accrete primarily from a stellar wind rather than Roche lobe overflow display increased X-ray absorption at phases $\phi \gtrsim 0.8$ (Haberl, White, & Kallman 1989, Heap & Corcoran 1992). This may be due to an accretion wake, a bow shock that results when the wind encounters the gravity of the compact object.

For both 4U 1700-37 and Vela X-1, increased absorption in optical lines is seen at late orbital phases. Accretion wakes are not expected to be as large as the primary star, so are probably not responsible. In Vela X-1, another structure caused by the interaction between the wind and the compact object, a photoionization wake, may cause the absorption (Kaper, Hammerschlag-Hensberge, & Zuiderwijk 1993). A photoionization wake has also been invoked to explain the asymmetry of the X-ray eclipse in Vela X-1 (Feldmeier et al. 1996). This wind structure was first described by Fransson & Fabian (1980), and is seen in two-dimensional hydrodynamic simulations (Blondin et al. 1991; Blondin 1994). Photoionization wakes result when the outflowing stellar wind in the shadow of the primary encounters the slower-moving wind that has been stalled by X-ray ionization. Only near the eclipse ingress line does the moving X-ray shadow of the star allow the fast-moving wind to continue to accelerate as it plows into the stalled wind.

The observations of X-ray dips and eclipses, however, have not provided us with information on the velocity field in the wind. For this, the UV P Cygni line profiles, formed by resonance scattering in the expanding wind, have proved useful. Hatchett & McCray (1977) pointed out that the P Cygni lines in a HMXB would vary over the binary orbit in a characteristic way. The ion responsible for the line would be removed from a region surrounding the X-ray source, so that at $\phi = 0.5$ the blue-shifted absorption would be diminished, while at $\phi = 0.0$ the red-shifted emission would be diminished. In general, the “transparency feature” in the P Cygni line would shift throughout the orbit depending on the velocity field of the wind. McCray et al. (1984) used this method to infer the mass-loss rate and terminal wind velocity of Vela X-1. Kaper et al. (1993) showed that the P Cygni

line variation in Vela X-1 suggests that the wind velocity does not increase monotonically with radius. A previous analysis of the P Cygni lines of LMC X-4 (Boroson et al. 1999) attempted to infer the radial velocity law from the orbital line variation.

While previous analyses of the wind velocity field from the Hatchett-McCray effect have been semi-empirical, two- and three-dimensional hydrodynamic simulations (Blondin et al. 1990, 1991; Blondin 1994) have been increasing in sophistication. Such models have been constructed for particular HMXB systems, and have been compared in some cases with X-ray observations (Blondin & Woo 1995; Wojdowski, Clark, & Kallman 1999). The empirical analysis of the UV lines is hampered by the many degrees of freedom required to describe the three-dimensional velocity and density fields of the wind. Greater physical insight can be provided if the hydrodynamic simulations are used to predict P Cygni profiles, which could then be compared with the observations. This has not been previously attempted, as most of the methods used to compute P Cygni lines have required the velocity and density fields to be spherically symmetric. Monte-Carlo simulation of P Cygni profiles (Stevens 1993; Knigge, Woods, & Drew 1995), however, is not subject to this limitation. In this paper we confront for the first time hydrodynamic models of stellar wind disruption by a compact object with observations of the UV P Cygni lines. We also calculate the differential emission measure in the model of wind and disk, and discuss the expected X-ray emission lines.

2. The Hydrodynamic Model

The hydrodynamical model used in this paper is a three-dimensional time-dependent numerical simulation of an HMXB first presented by Owen & Blondin (1997). The parameters of this model were chosen in accordance with the observed parameters of LMC X-4 (see Table 1). The high X-ray luminosity of LMC X-4 is difficult to reconcile with wind accretion alone, and the presence of a 30 day period in the X-ray light curve (Lang et al. 1981) and in the optical light curve (Heemskerk & van Paradijs 1989) suggests a precessing accretion disk fed by Roche lobe overflow.

2.1. Numerical Method

Our numerical model is an extension of previous models (Blondin et al. 1990, Blondin et al. 1991, Blondin 1994, Blondin & Woo 1995) used to study the dynamics of the circumstellar gas in HMXBs, and in particular the disruption of the normal OB stellar wind by the

compact X-ray source. These models are based on the time-dependent hydrodynamics code VH-1, and include (1) a radiatively driven stellar wind incorporated via the Sobolev approximation, (2) the X-ray photoionization of the wind as approximated by a cutoff of the radiative driving force, and (3) the X-ray heating and radiative cooling of the circumstellar gas.

The principal modification to this current model over that used in Blondin & Woo (1995) is the inclusion of the gravity of the compact X-ray source. This adds several features to the model, including tidal distortion of the primary, Roche lobe overflow leading to the formation of a tidal stream, the presence of an accretion disk, and a realistic mass accretion rate. In order to accurately model these features the spherical numerical grid (188 by 63 by 201 zones in r , θ , and ϕ) was structured to provide the highest spatial resolution near the surface of the distorted primary and near the accreting compact object.

The model is evolved only in one hemisphere, assuming reflection symmetry about the equatorial plane. In addition, a cone about the polar axis is removed from the simulation to reduce the number of time steps needed in the simulation. The use of an explicit hydrodynamics code restricts the time step to the smallest value of $\Delta x/v$ on the grid, where Δx is the width of a numerical zone, and v is a characteristic velocity (either the gas velocity or the sound speed). On a spherical grid Δx in the ϕ direction is given by $r \sin \theta \Delta \phi$. Therefore, as $\theta \rightarrow 0$, the zone width $\Delta x \rightarrow 0$ and $\Delta t \rightarrow 0$. Thus, to keep a reasonable value of Δt , we limited the simulation domain to $\theta > 0.3\pi$.

The numerical simulation was initialized with the surface of the primary star just inside the critical potential surface, such that the effective potential at the stellar surface was greater than the critical potential by one part in 10^5 . The boundary conditions on this surface correspond to an isothermal atmosphere in hydrostatic equilibrium. At the stellar surface temperature of 4×10^4 K, the scale height in this atmosphere is $\sim 10^9$ cm. From numerical experiments we found that VH-1 could simulate a stable atmosphere with zone spacing as large as twice the scale height; this is the value used in the present model. The density at this boundary is set at 5×10^{-9} g cm $^{-3}$, a value determined empirically to produce a stable stellar wind with the given parameters. The parameters describing the radiative driving force ($\alpha = 0.53$, $k = 0.12$; see e.g., Castor, Abbott & Klein 1975) were chosen based on the spectral type of the primary star. In the absence of a companion, this model would drive a spherical stellar wind with a mass loss rate of $\dot{M}_w \approx 2 \times 10^{-7} M_\odot \text{ yr}^{-1}$ and a terminal wind velocity of $v_\infty \approx 2000$ km s $^{-1}$.

The accretion-driven X-ray flux photo-ionizes, heats, and imparts momentum to the circumstellar gas. The X-ray luminosity was computed self-consistently as a function of the mass accretion rate onto the compact companion: $L_x = 0.1\dot{M}c^2$. This mass accretion rate,

\dot{M} , was computed by removing mass and energy from a block of 3^3 zones at the location of the companion (the zone size at this location is $\Delta x = 2.5 \times 10^9$ cm). However, the dense gas of the tidal stream and accretion disk are expected to be highly optically thick, and will shadow other regions of the binary system from this intense X-ray flux. To account for this shadowing in the simplest fashion, we computed the optical depth from the compact X-ray source to each numerical zone, and reduced the X-ray flux by $e^{-\tau}$. The reduced flux was used to calculate the local photoionization parameter, X-ray heating, and X-ray radiation pressure.

2.2. Simulation Results

The simulation was evolved for approximately one binary orbital period. This was sufficient time for the accretion disk to circularize and for the circumstellar gas to reach a state of quasi-equilibrium. By the end of the simulation there were five key features of the circumstellar gas: a radiatively driven wind from the shadowed surface of the primary star, a wind-compressed disk created by the rapid rotation of the primary star, a tidal stream emanating from the inner Lagrange point (L1), a Keplerian accretion disk around the compact object, and an X-ray irradiation driven wind emanating from the inner regions of the accretion disk.

The radiatively driven O-star wind fills a large fraction of the binary system due to the strong shadowing effects of the accretion disk. This normal stellar wind is marked by the presence of a wind-compressed disk (Bjorkman & Cassinelli 1993). The density of the wind in the equatorial plane is a factor of ~ 20 higher than at other latitudes. This effect is a direct result of assuming co-rotation between the primary star and the binary system; a slower stellar rotation would diminish or remove the wind-compressed disk.

The tidal stream is described remarkably well by the analysis of Lubow & Shu (1975). The tidal stream leaves the L1 point with an angle of $\sim 25^\circ$, in good agreement with the analytic prediction. The stream becomes supersonic only 10^{10} cm downstream, with the centroid of the stream following a ballistic trajectory until the stream impacts the disk. The gas in the stream continues to accelerate, reaching a Mach number at impact of ~ 16 .

The width of the tidal stream ($\sim 7 \times 10^{10}$ cm) is in good agreement with Lubow & Shu (1975); 70 % of the stream mass flux is within their quoted width. The stream cross section is consistently oblate, with the stream width being about 4/3 of the stream height. As shown by Lubow & Shu (1976), the vertical structure of the stream is determined entirely by the foot points of the streamlines in the tidal stream, and hence the stream has a scale

height much larger than that expected for hydrostatic equilibrium. The density in the tidal stream, and hence the mass transfer rate, is determined by the placement of the stellar surface relative to the L1 point (an arbitrary boundary condition in our model). Both the width of, and the density in, the tidal stream decrease as the stream accelerates toward the compact object.

By the end of the simulation the accretion disk has relaxed into a roughly steady-state configuration. The accretion flow has fully circularized and is nearly Keplerian, the vertical density profile matches that of an isothermal steady-state disk, and the outer radius is truncated at $\sim 8 \times 10^{10}$ cm, corresponding to $\sim 70\%$ of the Roche lobe of the compact object. Note, however, that the mass flux through the disk is not in equilibrium - even if such an equilibrium were possible in this numerical model, it would take far too long to reach.

The outer edge of the disk has a scale height of $\sim 2 \times 10^9$ cm, although the disk is somewhat thinner on the side nearest the primary star and fatter on the far side. This scale height is consistent with that of an isothermal accretion disk in steady state (the sound speed of the cold disk gas in our model is $c_s = 2.136 \times 10^6$ cm s $^{-1}$). The width of the tidal stream in the vicinity of the disk edge is noticeably wider, with a scale height of order $\sim 3 \times 10^9$ cm. As a result, a significant fraction of the tidal stream gas is not stopped at the disk edge, but rather flows over and under the disk along its surface. This stream overflow ultimately merges with the accretion disk in the vicinity of the point of closest approach: the location at which a ballistic trajectory from the L1 point would reach the closest to the compact companion.

In addition to the impact by the tidal stream, the outer edge of the disk is continually ablated by the strong stellar wind from the primary star. Note that this equatorial wind is enhanced by the wind compressed disk effect, and it is not directly affected by the X-ray source since it is shadowed by the accretion disk. As a result, the equatorial wind is strong enough to ablate a significant mass flux off the edge of the disk, particularly on the back side as seen in Figure 3. Furthermore, the ram pressure of this equatorial wind inflates the outer edge of the disk, creating a small outer rim that extends higher than the rest of the disk.

Although the outer regions of the disk are sufficiently resolved by our numerical grid, the inner regions of the disk are not. The scale height of a steady isothermal disk at a disk radius of 1.5×10^{10} cm should be $\sim 2.6 \times 10^8$ cm, but the limited resolution of our numerical model limits the disk thickness to values approximately three times larger. This limitation has direct bearing on the results of this paper in that this poor numerical resolution effectively limits (through the high opacity of the disk material) the cone of X-rays to a

smaller opening angle than if the disk were adequately resolved at small disk radii.

The intense X-ray luminosity of the accreting compact companion can influence the circumstellar gas in many ways, but in this numerical model the dominant effect is a strong bipolar wind driven off the inner region of the accretion disk via X-ray irradiation. The dense, cool gas on the surface of the accretion disk is heated by the incident X-ray flux to several million Kelvins. The ensuing high thermal pressure drives a strong wind with velocities reaching 2000 km s^{-1} . This irradiation is so intense in this numerical model that the X-ray flux striking the inner disk edge completely ablates the inner disk, leaving a substantial hole. As seen in Figure 4, this disk wind is roughly spherical. This has the interesting effect of producing a large volume of X-ray heated gas with a roughly constant ionization parameter. Since both the gas density and X-ray flux are decreasing as the square of the distance from the X-ray source, the ionization parameter in this gas remains at a constant value.

Because the poor numerical resolution in the inner accretion disk affects the vertical structure of the disk, the conservation of angular momentum in the disk gas, and the thermal transition of the X-ray heated gas, the geometry and mass flux in this bipolar wind is very uncertain. Nonetheless, it is clear from both simple order of magnitude estimates and from detailed calculations (de Kool & Wickramasinghe 1999) that the intense X-ray flux present in X-ray binaries will drive a substantial mass loss from the accretion disk.

Due to the shadowing effects of the accretion disk, the effects of X-ray photoionization are restricted to the bipolar disk wind in this model. Gas outside of the disk wind is shielded from the X-ray source, and as a result, there is no independent photoionization wake visible in this model. Instead, there is a relatively dense wake of circumstellar gas piled up along the leading surface separating the disk wind and the stellar wind. This modest wake, with a density contrast of ~ 4 , can be seen in the horizontal slices shown in Figure 5.

As seen in Blondin & Woo (1995), the radiatively-driven wind of the primary star is replaced by a thermally driven wind on the X-ray irradiated face of the primary. The high X-ray flux on the irradiated surface is strong enough to suppress the radiative driving force and quench the normal radiatively driven stellar wind. Instead, the X-ray flux heats the outer atmosphere of the star up to X-ray temperatures, and the ensuing high thermal pressure drives an outflow off the stellar surface. In this particular model, however, the thermally-driven stellar wind is effectively snuffed by the disk wind. The momentum in the disk wind is sufficiently high that it stops the stellar wind before it can reach a sonic point. This subsonic outflow is then redirected up over the top of the star along with the supersonic disk wind. This dynamical interaction between star and disk winds can be seen in Figure 3.

3. Monte Carlo Simulation of P Cygni Profiles

Because the density and velocity fields $\rho(r, \theta, \phi)$ and $\mathbf{v}(r, \theta, \phi)$ given by the hydrodynamic model are not spherically symmetric, we cannot use an escape probability method (Castor 1970; Castor & Lamers 1979) or the Sobolev with Exact Integration method (Lamers, Cerruti-Sola, & Perinotto 1987) to compute the P Cygni line profiles. The lines we consider are doublets separated by wavelengths less than the terminal wind velocity. Thus photons emitted by one doublet component can be scattered by the other, coupling different regions of the wind. To circumvent the difficulty of solving the radiative transfer integrals in this situation, we apply a Monte-Carlo method similar to that of Knigge, Woods, & Drew (1995). Unique features of our method are discussed in Appendix A. We show tests of our program in the Appendix B.

3.1. Method

We start the simulation by following a photon emitted by a random point on the star’s surface. (The emission from the accretion disk should be dominated by emission from the primary. For the UV continuum, the disk contributes only $\approx 8\%$). The random point is chosen with a weighting that takes into account the gravity darkening appropriate for a high-mass star with a radiative, rather than convective, atmosphere. The photon’s initial direction is chosen randomly, but for the frequency ν , we step through a range centered on the rest frequency ν_0 with a width given by the maximum wind velocity. The details of the simulation are generally similar to those used by Knigge, et al. (1995). Because the wind velocity is not smooth or monotonic down to scales on the order of the grid spacing of the hydrodynamic simulation, we cannot solve exactly for a resonant point along the photon’s path in which $\nu = \nu_0(1 + \mathbf{v}_{\text{wind}} \cdot \mathbf{n}_{\text{photon}}/c)$. To work around this, we allow a microturbulent velocity within the wind. (For a treatment of microturbulence using the Sobolev approximation for the source function in a spherically symmetric wind, see Lamers, Cerruti-Sola, & Perinotto 1987). In addition to the practical benefit of allowing substantial optical depths at nonresonant points, allowing microturbulence may also simulate turbulent motions on a scale smaller than that of our numeric grid. The value of the microturbulent velocity that we chose based on the thermal velocity and the deviation in velocity among neighboring grid points is 4% of the terminal velocity. Such a turbulent velocity does not cause a dramatic change in the P Cygni profiles of symmetric winds.

3.2. Auxiliary Assumptions

In order to predict P Cygni profiles from the density and velocity fields computed by the hydrodynamic simulation, we need to make several auxiliary assumptions.

First, we must assume abundances for Carbon and Nitrogen; these are given in Table 1. Although metal abundances in the LMC are generally 20% of galactic abundances, we have chosen enhanced abundances because the observed N V and C IV lines are much stronger than expected from a star of the spectral type of LMC X-4. As we will see in §4, this assumption has negligible effect on our conclusions.

Second, we must determine the ionization stage of the wind both in the presence and absence of X-ray illumination from the compact object. In the absence of X-ray illumination, we use an empirical relation

$$\tau_E = T(1 + \gamma)r^{-\gamma} \quad (1)$$

for the radial optical depth τ_E . This parameterization is often used to fit OB star spectra (Castor & Lamers 1979). We used values of T and γ that we used in Boroson et al. (1999) to fit the lines observed with the GHRS (see Table 1). In view of the deep absorption troughs seen at $\phi = 0.08$ and $\phi = 0.9$ (atypical for an O7-9III-V star), we allowed an additional source of ionization. LMC X-4 is known to show a residual X-ray flux during eclipse that is $\approx 1\%$ of its maximum level (Woo et al. 1995), presumably due to Thompson scattering of X-rays in the wind. We determined the ionization stage of the wind in response to the scattered X-rays using the XSTAR photoionization code (Kallman et al. 1996). Using the observed X-ray spectrum of LMC X-4 diluted to 1% of the total luminosity, we found the fraction of N V and C IV for various values of the ionization parameter $\xi \equiv L_x/n_e r^2$, where r is the distance from the X-ray source to the point in the wind, L_x is the X-ray luminosity, and n_e is the electron density. The optical depth then follows from the Sobolev approximation:

$$\tau_S = (\pi e^2/mc)f\lambda_0 n_{i,j}(dv/dr)^{-1} \quad (2)$$

where e is the electron charge, m is the electron mass, λ_0 is the rest wavelength of the transition, f is the oscillator strength, $n_{i,j} = (n_e/\mu)a_i g_j$ is the number density of element i in ionization stage j , $\mu = 1.2$ is the ratio of the mean atomic mass to that of hydrogen, and dv/dr is the wind velocity derivative in the direction of the photon's path. For the optical depth in the wind we then choose whichever of τ_E or τ_S is greater.

In the presence of X-ray illumination (outside the X-ray shadow of the normal star), we again compute τ_E and τ_S , but now we compute τ_S using the ion fractions given by X-ray illumination by the full luminosity of LMC X-4 (self-consistently calculated from the

accretion rate of the simulation to be 2×10^{38} erg s⁻¹). We now use whichever of τ_E or τ_S is less.

As the simulation includes dense areas of the wind near the stellar photosphere, the gas stream, and the accretion disk, collisional de-excitation can prevent photons from scattering. This causes the absorption lines that we modelled empirically with Gaussians in Boroson et al. (1999). Our treatment of the stellar absorption (see Appendix A) is necessarily approximate, as the hydrodynamic simulation does not fully resolve the stellar atmosphere. The predictions of the line profiles at low velocity, where the stellar absorption is strong, should therefore be considered approximate.

3.3. Limitations of the Model

The hydrodynamic model was constructed in order to study the Roche lobe overflow and formation of the accretion disk. For these purposes, the simulation did not need to extend beyond 2.5 stellar radii. We have not attempted to extrapolate the wind density and velocity fields beyond $2.5R_*$. For a standard $\beta = 0.8$ stellar wind velocity law, that is

$$v(r) = v_\infty(1 - R_*/r)^\beta, \quad (3)$$

the wind only reaches 66% of its terminal velocity at the edge of the grid.

The region about the poles of the normal star was excluded from the simulation; the grid only extended from spherical coordinate $\phi = 52^\circ$ to $\phi = 90^\circ$. We simply interpolated the density and temperature fields across the polar region; this should be accurate enough for our current purposes, as this region does not include the accretion wake, photoionization wake, stream, or disk. The simulation only includes the region above the orbital plane. When a photon passes below this plane in our simulation, it encounters density and velocity fields that are reflections of those above the plane.

4. Results

4.1. Orbital Variation of P Cygni Lines

We compare the results of the simulation with the N V $\lambda\lambda 1238, 1242$ and C IV $\lambda\lambda 1548, 1550$ lines observed with the GHRS and STIS aboard the Hubble Space Telescope (Figures 6 and 7). The model spectra have errors in each 60 km s⁻¹ bin (determined from photon counting Poisson statistics of the Monte Carlo simulation) of $\approx 5\%$ of the flux. For the STIS spectra, the errors are $\approx 1\%$ in each 30 km s⁻¹ bin.

The simulations reproduce qualitatively the observed Hatchett-McCray effect. The absorption of the N V and C IV lines is reduced at $\phi = 0.5$. In agreement with observations, the simulations predict some N V absorption remaining at $\phi = 0.5$. This results from a combination of true absorption (collisional de-excitation) and scattering from the photosphere and dense regions of the wind that are not fully ionized even when exposed to X-rays.

The orbital variability depends on the ratio L_{38}/\dot{M}_{-6} , where L_{38} is the X-ray luminosity in units of 10^{38} erg s $^{-1}$ and \dot{M}_{-6} is the mass-loss rate in units of 10^{-6} M_{\odot} yr $^{-1}$. In Boroson et al. (1999), we fit the P Cygni lines observed with the GHRS to find $L_{38}/\dot{M}_{-6} = 0.26 \pm 0.01$ for a homogeneous wind or $L_{38}/\dot{M}_{-6} = 0.7 \pm 0.4$ for a two-component wind with a density contrast 700 ± 200 . In the hydrodynamic simulation, L_{38} is fixed at 2, and $\dot{M}_{-6} = 0.1 - 0.2$ (similar to the value found by Woo et al. 1995). However, we note that the simulated wind is highly inhomogeneous. While 50% of the wind volume has a local $\dot{M}_{-6} = 0.05 - 0.2$ (determined from continuity), 50% of the wind mass is in clumps denser by factors ≈ 2000 . These clumps are found mostly in the wind-compressed disk.

We investigated whether observable features in the P Cygni profiles could be traced to structures predicted by the hydrodynamic simulation. To do this, we simulated the P Cygni lines from a stellar wind first with a spherically symmetric v field given by Equation 3 and the same density field given by the simulation, and then with both a spherically symmetric velocity field and a spherically symmetric density field given by the continuity equation with $\dot{M} = 1.5 \times 10^{-7}$ M_{\odot} yr $^{-1}$.

The model predicts slightly greater absorption at $\phi = 0.3$ than at $\phi = 0.7$ (Figure 8) as a result of the aspherical wind density. The enhancement of the red-shifted emission at $\phi = 0.7$ over $\phi = 0.3$ (for both N V and C IV) results from the detailed velocity field of the hydrodynamic simulation (not merely the effect of the binary rotation). For a wind with spherical symmetry and homogeneous density, the ratio of the apparent optical depths in the absorption at the blue doublet component to the absorption at the red doublet component is 2 : 1. In the inhomogeneous wind of the simulation, partial covering of the star by dense clumps allows the doublet ratio to approach a $\approx 3 : 2$ ratio (determined from the profiles given by our Monte Carlo calculation) even when the apparent optical depth $\tau \gg 1$. By the apparent optical depth we mean $-\log F_{\lambda}$, where F_{λ} is the continuum-normalized flux at wavelength λ . This is only an apparent optical depth because the flux at λ is the sum of fluxes from different sightlines with different optical depths.

There are no signatures of the disk wind seen in Figure 4 in the P Cygni profiles, as this wind is ionized to stages higher than N V and C IV by the unabsorbed X-rays escaping perpendicular to the disk plane.

Some discrepancies between the data and model result from the radial cutoff ($2.5R_*$) and the terminal velocity (2000 km s^{-1}) used in the simulation ($v_\infty = 1150 \text{ km s}^{-1}$ fits the data better). For example, the maximum observed velocity is $v_{\text{max}} = v_\infty(1 - 1/r_{\text{max}})^\beta$. Although the simulation predicts the observed v_{max} at $\phi = 0.08$, this results from too large a value for v_∞ and too small a value for r_{max} (which should approach infinity). At $\phi = 0.2 - 0.3$, when the X-rays ionize the wind at large radii, the simulation predicts absorption in the wind at too high a velocity. For the C IV line, using too large a value for v_∞ results in a merging of the two doublet components.

The simulated profiles do *not* show the orbital asymmetry seen in IUE equivalent widths (Boroson et al. 1999) or in the HST STIS spectra (more absorption is seen for $0.5 < \phi < 1.0$ than for $0.0 < \phi < 0.5$). This is shown clearly for the case of N V in Figure 8. Although we have made two assumptions designed to increase the ion fraction of N V (that the N abundance is not depleted as it is for many LMC stars, and that scattered X-rays can increase the ion fraction), we still find that the model does not reproduce the saturated N V absorption lines at $\phi = 0.90$. In order to produce saturated absorption, the absorbing material must cover the entire stellar surface.

The presence of a He II ionization front (Masai 1984) may invalidate our use of simple scaling with ξ . That is, at distances far enough from the X-ray source, a large fraction of He (which has high abundance) is in the form He II, and is efficient at absorbing X-rays with $E > 55 \text{ eV}$. The potential for ionizing N V to higher stages is 98 eV . X-ray ionization would not be efficient at ionizing N V to higher stages if 98 eV photons are absorbed by He II.

A full treatment of the optically-thick ionization balance is beyond the scope of this paper. We point out, however, that when we apply Equation 15 of Masai (1984) to the wind in LMC X-4, we find that the He II ionization front would be at about 10 stellar radii from the neutron star, outside of the grid of the hydrodynamical simulation. In the LMC X-4 system, the X-ray luminosity is higher and the orbit is more compact than for Vela X-1, for which Masai’s analysis may be more appropriate. This assumes a smooth wind with parameters given by the spatially averaged values of the simulation. Absorption by He II in an inhomogeneous wind may in general be more important. Most of the inhomogeneity in the present simulation is in the wind-compressed disk about the normal star. We have found that the X-ray ionization effect is mostly confined to the ionization of the accretion disk wind, as elsewhere the wind is in the shadow of either the disk or the star. The disk wind should have a nearly constant ionization parameter $\log \xi > 5$ so that He II should not cause much absorption within this region. Although an ionization front may decrease the effects of X-ray ionization on N V and C IV, it is unlikely to do so in a manner asymmetric enough to cause the phase asymmetry in the P Cygni profiles (Figure 8).

4.2. Random Variability of P Cygni Lines

We also simulated the P Cygni line variability using density and velocity fields given by a second frame of the hydrodynamic simulation, to get a sense for how much P Cygni variability is to be expected from the “weather” of the system. The time interval between the two frames, 3300 seconds, is approximately the same as the length of an HST orbit, and approximately the flow time across one stellar radius.

The result of the comparison of P Cygni profiles, shown in in Figure 9, shows that the random variability does not exceed that expected from our simulated photon statistics, $\approx 5\%$ of the flux in each 60 km s^{-1} wavelength bin. Thus if these simulations are representative, it should be safe to assume that variability in the line profiles throughout a binary orbit is a reflection of changes in the orientation of the wind and not random variability of the density and velocity fields.

4.3. X-ray Spectra of the Wind

From the density, temperature, and ionization in the hydrodynamic model, we can also predict the contribution of the wind to the X-ray spectrum. This should include recombination and fluorescent lines from the X-ray illuminated wind, Compton scattering of the X-ray continuum from the neutron star, and thermal bremsstrahlung emitted by the hot wind. Following the method of Wojdowski et al. (1999), we determine the recombination and fluorescent spectra at each point in the wind from the local ξ , the sum of a blackbody and a cut-off power law approximation to the LMC X-4 X-ray spectrum, and the XSTAR code. For the bremsstrahlung spectrum, we use the temperature field of the hydrodynamic model instead of the temperature calculated from XSTAR, as the wind can also be heated by shocks. We propagate the wind spectrum along the line of sight, and allow absorption by the ionized wind and by an interstellar column density of neutral gas $N_H = 10^{21} \text{ cm}^{-2}$. We assume a distance to LMC X-4 of 50 kpc, and a system inclination of 65° .

We show the simulated mid-eclipse spectrum, its separate components, and the observed ASCA spectrum from the campaign reported in Vrtilik et al. (1997) in Figure 10. The predicted spectrum, which we have folded with the ASCA response, is due almost entirely to Compton scattering. If we fit the observed spectrum with the model with arbitrary normalization, we find the observed spectrum is a factor of 4 brighter than that predicted. We also computed the wind spectra at $\phi = 0.25, 0.50, 0.75$, but found no strong line features.

Recombination and fluorescent lines provide a negligible contribution because the

disk shadows much of the wind. Wojdowski et al. (1999) found that the hydrodynamic simulation of the wind in SMC X-1 predicts *greater* recombination flux than is observed, and suggested this could result from a low metal abundance ($Z < 3 \times 10^{-2}$). Wojdowski et al. (1999) did not take into account the absorption of X-rays from the central source to the wind. No accretion disk was present in the SMC X-1 simulation, although the high X-ray luminosity and the long-term period are evidence that one exists. The under-prediction of X-rays in mid-eclipse by the LMC X-4 simulation could result from too thick an accretion disk.

5. Future Work

Some of the detailed predictions of the hydrodynamic model do not match observations. In particular, the observed absorption troughs are deeper than predicted by our simulations at $\phi = 0.68, 0.90$, and are deeper than observed at $\phi' = 1 - \phi$.

We plan to revise the boundary conditions of the simulation to see if the observed line features can be reproduced. The first adjustments to be made should be minor adjustments to the current model: we know, for example, that the terminal velocity of the wind should be closer to 1000 km s^{-1} than 2000 km s^{-1} . The mass-loss rate may also be higher than the $1 - 2 \times 10^{-7} M_{\odot} \text{ yr}^{-1}$ used in the simulation. Both of the parameters depend on the details of the line-scattering responsible for the wind acceleration, parameterized by κ and α in Castor, Abbott, & Klein (1975). The values of κ and α for the O star may differ from that assumed for the simulation because of the different abundances in the LMC and in the Galaxy, or because of the evolutionary status of the star.

If the mass-loss rate \dot{M} were higher than that assumed in the simulation, the P Cygni absorption would be greater. Two effects combine to increase τ in Equation 2. With a higher value of \dot{M} , $n_{i,j} = (n_e/\mu)a_i g_j$ is increased both because n_e is increased on average (by conservation of mass) but also because g_j , the fraction of ions in the absorbing stage is increased as well. However, the effects of an altered \dot{M} on the hydrodynamics remain to be investigated.

One possible explanation for the enhanced absorption at $\phi > 0.5$ is that a photoionization wake is present. The simulations show a similar wake at high stellar latitudes (Figure 5), but the wake does not wind around the star to cause absorption at $\phi \approx 0.9$. We will extend the simulation to radii $R > 2.5R_*$ to determine whether the restricted size of the simulation grid has prevented a larger wake from forming.

The photoionization wake does not form at lower latitudes because the disk prevents

X-rays from ionizing the wind in the orbital plane. The half-angle of the simulated disk is $\approx 8^\circ$, but the X-rays are shadowed from a half-angle of $20 - 30^\circ$ by structures in the inner disk. For all reasonable values of the orbital inclination, the disk shape determined from the simulation prevents direct X-rays from the neutron star from being observed at the Earth. This is consistent with the lack of X-rays for ≈ 0.5 of the 30 day cycle, but is clearly inconsistent with the detection of X-ray pulses and a flux implying near-Eddington luminosities during the rest of the cycle. In future models, we will improve the spatial resolution of the inner accretion disk, to more accurately model the disk structure and X-ray illumination. This will allow X-rays to be visible at Earth for some disk inclinations, and may allow a photoionization wake to form over a larger region.

We will also explore the effects of nonsynchronous rotation of the primary star on the hydrodynamic flow. The width of optical lines (Hutchings et al. 1978) suggests the O star rotates at about half of the orbital frequency. Levine et al. (1999) measured the orbital period derivative to be $\dot{P}_{\text{orb}}/P_{\text{orb}} = (-9.8 \pm 0.7) \times 10^{-7} \text{ yr}^{-1}$, and argued, citing similar arguments for the SMC X-1 system, that this results from tidal forces operating only for nonsynchronous rotation. If the primary does not corotate, then the wind may be launched with an angular velocity (in the rotating frame) that enhances the absorption at $\phi = 0.9$.

We expect that the comparison of global hydrodynamic models with observations will continue to test our understanding of disks, winds, and their interactions.

A. Appendix: The Monte-Carlo Simulation and its Treatment of Microturbulence

Our method follows that of Knigge et al. (1995). We follow randomly scattering “photons” that are actually representative samples of many photons. A weight assigned to each “photon” determines its relative contribution to the final profile. When there is some probability for a scattering to take place and some probability for the photon to escape the system, the photon scatters, but its weight is multiplied by the scattering probability. Photons emitted on the stellar surface have some small probability ϵ of entering our line of sight. As every photon we see must eventually enter our line of sight, we allow one probability- ϵ event to occur each time a photon is emitted or scattered isotropically. However we no longer follow the path of photons scattered away from our line of sight, as their contribution should be $\sim \epsilon^2$, negligibly small.

For each randomly chosen point on the stellar surface we perform an integration along the line of sight. The photon’s initial weight is μ , the cosine of the angle between the surface

normal and the line of sight. When we tally the weights of the photons reaching the observer for a given ν , we normalize based on the weights μ that were emitted. Those photons that are not initially headed towards the observer are all given a weight of unity, but the distribution of their random directions is chosen to take into account the different fluxes received at various angles. At each scattering, there is again a probability of ϵ that it enters the line of sight, so we propagate the photon along the line of sight and collect its weight into frequency bins to form the spectrum. When a photon excites a resonance line, there is a probability of $1/[1 + n_e q_{21}/A_{21}]$ that the excited atom will decay through re-emission and not collisions. Here, A_{21} is the Einstein A coefficient and $q_{21} = 8.629 \times 10^{-6} \Sigma / (T^{1/2} g)$ is the decay rate per ion, with the “collision strength” $\Sigma \approx 8$ (Clark et al. 1982), and g defined as the statistical weight of the upper level.

Microturbulence affects the Monte-Carlo simulation in two ways. First, the probability that a photon is scattered along the line of flight from p to p' is $1 - \exp(-\tau)$, with

$$\tau = \int_p^{p'} (\kappa_B + \kappa_R) ds \quad (\text{A1})$$

Here, κ_B (κ_R) is the scattering coefficient in the blue (red) doublet component, given by

$$\kappa = \kappa_0 \exp(-\Delta w^2) / \pi \Delta w_T \quad (\text{A2})$$

where $\Delta w_T = v_T / v_\infty$ is the normalized 1σ microturbulent velocity and Δw is given by

$$\Delta w_B = (c/v_\infty)(\nu - \nu_0)/\nu_0 - \mathbf{V} \cdot \mathbf{n} \quad (\text{A3})$$

for the blue doublet component and $\Delta w_R = \Delta w_B + \delta$ for the red doublet component. The factor κ_0 is set to the optical depth in Equations 1 or 2, with the derivatives taken with respect to the line of flight distance s rather than the radius r from the center of mass of the primary star (radial optical depths converted to line-of-flight optical depths). Once it is determined that a photon scatters along a flight line, the scattering point is determined by the method of Knigge et al., and the probability that the photon is scattered by the blue (red) doublet component is κ_B/κ (κ_R/κ) where $\kappa = \kappa_B + \kappa_R$.

Second, a photon’s frequency ν is altered following a scattering, depending on the microturbulent velocity distribution width Δw_T . Given that the macroscopic velocity field has a velocity vector $\mathbf{V}(r, \theta, \phi)$ at point p and that the line of flight is defined by the unit vector \mathbf{n} , the actual microturbulent velocity \mathbf{v}_T at point p that scatters the photon must have a component along the line of flight $\mathbf{v}_T \cdot \mathbf{n} = \Delta w$ (if the red component has scattered the line then $\mathbf{v}_T \cdot \mathbf{n} = \Delta w + \delta$). Then the velocities in two directions perpendicular to \mathbf{n} are given by $v_\infty \Delta w_T \Phi$, where Φ is a random number with Gaussian distribution. The

frequency of the scattered photon is then $\nu' = \nu_0(1 + \mathbf{v}_{\text{wind}} \cdot \mathbf{n}/c)$ for the blue component and $\nu' = (\nu_0 - \delta)(1 + \mathbf{v}_{\text{wind}} \cdot \mathbf{n}/c)$ for the red component. Here, $\mathbf{v}_{\text{wind}} = \mathbf{V}(r, \theta, \phi) + \mathbf{v}_T$ is the actual velocity vector of the ion that scatters the photon.

B. Appendix: Comparison of the Monte Carlo code and the SEI and Comoving Frame methods

In this Appendix, we show that our Monte Carlo P Cygni profile code can reproduce the results of calculations in the literature using the SEI method (Lamers et al. 1987) or the Comoving Frame method (Hamann 1981). We calculate P Cygni profiles for the wind velocity law

$$w(x) = (1 - 0.999/x)^{0.5} \tag{B1}$$

where $w(x) = v(x)/v_\infty$, and $x = R/R_*$. We use a uniform microturbulent velocity $\Delta w_T = 0.1$ and a doublet separation $\delta = (\nu_B - \nu_R)c/\nu_B v_\infty = 0.7$. The doublet ratio is assumed to be 2:1 (the oscillator strength in the blue component being greater.) We make two tests; one for $\tau_B = 1$, and the other for $\tau_B = 20$. The second is a more stringent test, as the typical photon undergoes more scatterings, and errors introduced at each scattering are magnified. For the results of the Comoving Frame method, we use the values plotted in Fig. 6 of Lamers et al. For the results of the SEI method, we use profiles computed with our own version of the SEI code, which we applied to the LMC X-4 system in Boroson et al. (1999).

For these tests, we use a spherical star. In contrast to the case in which the star fills its Roche lobe, here we know exactly the fraction of line-of-sight photons that do not intersect the stellar surface (that is, we know the visible surface area of the star exactly.) Thus the continuum level is known, and the number of photons initially emitted along of the line of sight that arrive at each frequency is normalized to this continuum level. The photons that have scattered into our line of sight are normalized to the total number emitted by the star.

We show the results of the comparison of the three methods in Figure 11. The rms deviation between the SEI and Monte Carlo methods is 3% for $\tau = 1$ and 7% for $\tau = 20$.

We would like to thank Daniel Proga, Lex Kaper, Patrick Wojdowski, and Masao Sako for useful discussions. This work was based on observations with the NASA/ESA *Hubble Space Telescope*, obtained at the Space Telescope Science Institute, which is operated by the Association of Universities for Research in Astronomy, Inc., under NASA contract GO-05874.01-94A. BB acknowledges an NRC postdoctoral associateship. JMB

acknowledges an NSF CAREER Award.

REFERENCES

- Abbott, D.C. 1980, *ApJ*, 242, 1183
- Bjorkman, J. E. & Cassinelli, J. P. 1993, *ApJ*, 409, 429
- Blondin, J.M. 1994, *ApJ*, 435, 756
- Blondin, J.M., Stevens, I.R., & Kallman, T.R. 1991, *ApJ*, 371, 684
- Blondin, J.M., Kallman, T.R., Fryxell, B.A., & Taam, R.E. 1990, *ApJ*, 356, 591
- Blondin, J.M., & Woo, J.W. 1995, *ApJ*, 445, 889
- Bondi, H., & Hoyle, F. 1944, *MNRAS*, 104, 273
- Boroson, B., Kallman, T., McCray, R., Vrtilik, S.D., & Raymond, J. 1999. *ApJ*, 519, 191
- Castor, J. 1970, *MNRAS*, 149, 11
- Castor, J.I., Abbott, D.C., & Klein, R.I. 1975, *ApJ*, 195, 157
- Castor, J., & Lamers, H.J.G.L.M., 1979, *ApJS*, 39, 481
- Clark, R.E.H., Magee, N.H. Jr., Mann, J.B., & Merts, A.L. 1982, *ApJ*, 254, 412
- Feldmeier, A., Anzer, U., Boerner, G., & Nagase, F. 1996, *A&A*, 311, 793
- de Kool, M. & Wickramasinghe, D. 1999, *MNRAS*, 307, 449.
- Fransson, C. & Fabian, A.C. 1980, *A&A*, 87, 102
- Haberl, F., White, N.E., & Kallman, T.R. 1989, *ApJ*, 343, 409
- Hamann, W.R. 1980, *A&A*, 84, 342
- Hatchett, S.P. & McCray, R. 1977, *ApJ*, 211, 552
- Heap, S.R., & Corcoran, M.F. 1992, *ApJ*, 387, 340
- Heemskerk, M.H.M. & van Paradijs, J. 1989, *A&A*, 223, 154
- Ho, C., & Arons, J. 1987, *ApJ*, 321, 404
- Hutchings, J.B., Crampton, D., & Cowley, A.P. 1978, *ApJ*, 225, 548
- Kallman, T., Liedahl, D., Osterheld, A., Goldstein, W., & Kahn, S. 1996, *ApJ*, 465, 994
- Kaper, L, Hammerschlag-Hensberge, G., & Zuiderwijk, E.J. 1994, *A&A*, 289, 846
- Kaper, L., Hammerschlag-Hensberge, G., & van Loon, J.Th. 1993, *A&A* 279, 485
- Kelley, R.L., Jernigan, J.G., Levine, A., Petro, D., Rappaport, S.A. 1983, *ApJ*, 264, 568
- Knigge, C., Woods, J.A, & Drew, E. 1995, *MNRAS*, 273, 225
- Lamers, H.J.G.L.M., Cerruti-Sola, M., & Perinotto, M. 1987, *ApJ*, 314, 726

- Lang, F.L., Levine, A.M., Butz, M., Hauskins, S., Howe, S., Primini, S.A., Lewin, W.H.G.,
Baity, W.A., Knight, F.K., Rothschild, R.E., Petterson, J.A. 1981, ApJ, 246, L21
- Levine, A., Rappaport, S., Putney, A., Corbet, R., & Nagase, F. 1991, ApJ, 381, 101
- Levine, A.M., Rappaport, S.A., & Zojcheski, G. 1999, ApJ, submitted, astro-ph/9911173
- Lubow, S. H. & Shu, F. H. 1975, ApJ, 198, 383
- Lubow, S. H. & Shu, F. H. 1976, ApJ, 207, L53
- Lucy, L.B., & White, R.L. 1980, ApJ, 241, 300
- MacGregor, K.B., & Vitello, P.A.J. 1982, ApJ, 259, 267
- MacGregor, K.B., Hartmann, L., & Raymond, J.C. 1979, ApJ, 231, 514
- Masai, K. 1984, Ap&SS, 106, 391
- McCray, R., Kallman, T.R., Castor, J.I., & Olson, G.L. 1984, ApJ, 282, 245
- Owen, M. P. & Blondin, J. M. 1997, in *Accretion Phenomena and Related Outflows; IAU
Colloquium 163*, eds D. T. Wickramasinghe, G. V. Bicknell & L. Ferrario, p. 779
- Owocki, S.P., & Rybicki, G.B. 1984, ApJ, 284, 337
- Owocki, S.P., Castor, J.I. & Rybicki, G.B. 1988, ApJ, 335, 914
- Stevens, I.R. 1993, ApJ, 404, 281
- Vrtilek, S.D., Boroson, B., McCray, R., Nagase, F., & Cheng, F. 1997, ApJ, 490, 377
- Wojdowski, P.S., Clark, G.W., & Kallman, T.R. 1999, ApJ, in press
- Woo, J.W., Clark, G.W., & Levine, A.M. 1995, ApJ, 449, 880
- Woo, J.W., Clark, G.W., Levine, A.M., Corbet, R.H., & Nagase, F. 1996, ApJ 467, 811

Fig. 1.— An isodensity surface of the hydrodynamic model at the end of the numerical simulation, illustrating the relative scales of the accretion disk, tidal stream and primary star.

Fig. 2.— A two-dimensional slice along the line of centers of the binary system illustrating the five key components of the circumstellar gas.

Fig. 3.— The velocity field of the circumstellar gas in the equatorial plane of the binary system. Here black represents the relatively low density of the equatorial wind, while white represents the high density of the primary star, tidal stream, and accretion disk. The solid line marks the critical potential surface.

Fig. 4.— The bipolar disk wind emanating from the inner region of the accretion disk is evident in this two-dimensional slice along the line of centers of the binary system. Note that the disk wind crashes into an irradiation-driven wind off the surface of the primary star.

Fig. 5.— The influence of the disk wind on the circumstellar structure is seen in these two-dimensional slices parallel to the equatorial plane. The density in the leading wake (left of the disk wind) is 4 times higher than the normal stellar wind at that radius. Note that in the top slice the inner edge of the grid is beyond the surface of the primary star.

Fig. 6.— Simulated N V P Cygni profiles from LMC X-4 (solid lines), assuming density and velocity fields given by hydrodynamic simulations, compared with P Cygni profiles observed with the STIS or GHRS (dotted lines). Velocities are relative to the velocity of the LMC (280 km s^{-1} redshift) and are scaled to a maximum wind velocity of 2000 km s^{-1} . Exposures at $\phi = 0.08, 0.28, 0.53, 0.68, 0.90$ were obtained with the STIS, while exposures at $\phi = 0.11, 0.21, 0.31, 0.41$ were obtained with the GHRS

Fig. 7.— Simulated C IV P Cygni profiles from LMC X-4 (solid lines), assuming density and velocity fields given by hydrodynamic simulations, compared with spectra observed with the STIS or GHRS (dotted lines). Exposures at $\phi = 0.08, 0.28, 0.53, 0.68, 0.90$ were obtained with the STIS, while exposures at $\phi = 0.16, 0.26, 0.36, 0.46$ were obtained with the GHRS.

Fig. 8.— Examination of the orbital asymmetry in the N V line profiles. From X-ray ionization alone, the profiles at $\phi, 1 - \phi$ should be identical. The top left panel shows that the profile at $\phi = 0.08$ (solid line) does not have as much absorption as the profile at $\phi = 0.90$ (dotted line). The bottom left panel compares the profiles at $\phi = 0.28$ (solid line) and $\phi = 0.68$ (dotted line). Panels on the right show the predictions from the simulations.

Fig. 9.— Differences between N V profiles predicted from the simulation at two time frames. The dotted line shows the expected error from the simulated counting statistics.

Fig. 10.— The X-ray spectrum expected from the wind in mid-eclipse in the simulation and as observed with ASCA. The error bars and limits show the ASCA data, while the Compton-scattered, bremsstrahlung, recombination line, and fluorescent line spectra folded with the ASCA response are indicated by “Compt”, “Brems”, “Recom”, and “Fluor”.

Fig. 11.— A comparison of the results of our Monte-Carlo P Cygni line simulation (solid line) with the results of the SEI method (+ signs) and Comoving Frame method (\diamond signs.) Top panel: optical depths $\tau_B = 20, \tau_R = 10$. Bottom panel: $\tau_B = 1, \tau_R = 0.5$.

Parameter name	Meaning	Value	Reference
L_x	X-ray luminosity	$2 \times 10^{38} \text{ erg s}^{-1}$	*
M_O	Mass of O star	$14.6 M_\odot$	*(4)
M_{ns}	Mass of neutron star	$1.4 M_\odot$	*(4)
P_{orbit}	Orbital period	1.4 d	3
i	Orbital inclination	65°	*(3,4)
a	Separation of centers of mass	$9.35 \times 10^{11} \text{ cm}$	*(3,4)
	Spectral type	O 7III-V	2
a_N	Nitrogen abundance	10^{-4}	*
a_C	Carbon abundance	3.6×10^{-4}	*
γ	Wind depth exponent	0.75	1
T	Total wind depth	1.15	1
v_T/v_∞	Turbulent velocity	0.04	*

Table 1: Adopted parameters of the LMC X-4 system

*Adopted

¹Borson et al. 1999

²Hutchings, Crampton, & Cowley 1978

³Kelley et al. 1981

⁴Levine et al. 1991

Fig. 1.— See JPEG file

Fig. 2.— See JPEG file

Fig. 3.— See JPEG file

Fig. 4.— See JPEG file

Fig. 5.— See JPEG file

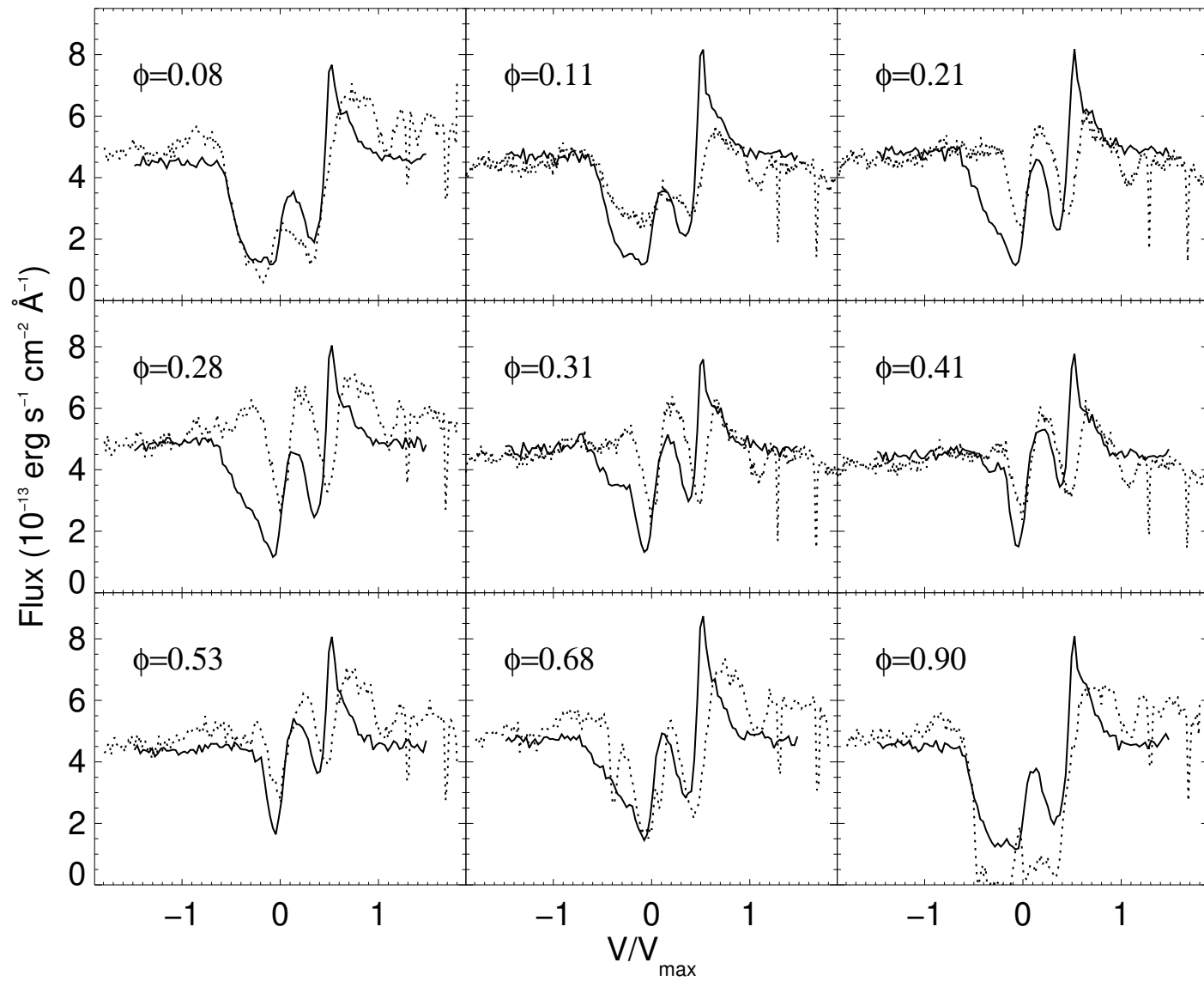


Fig. 6.—

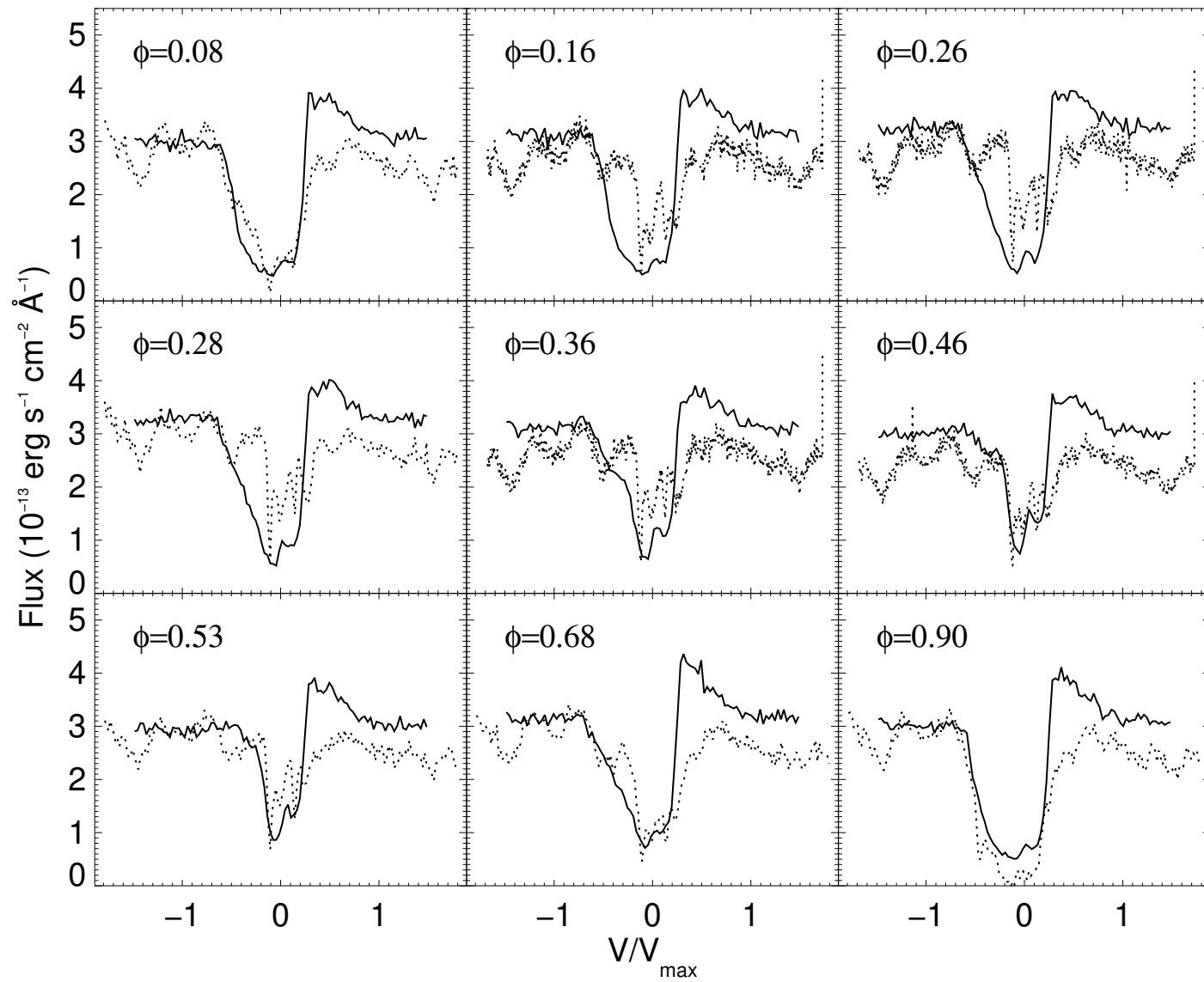


Fig. 7.—

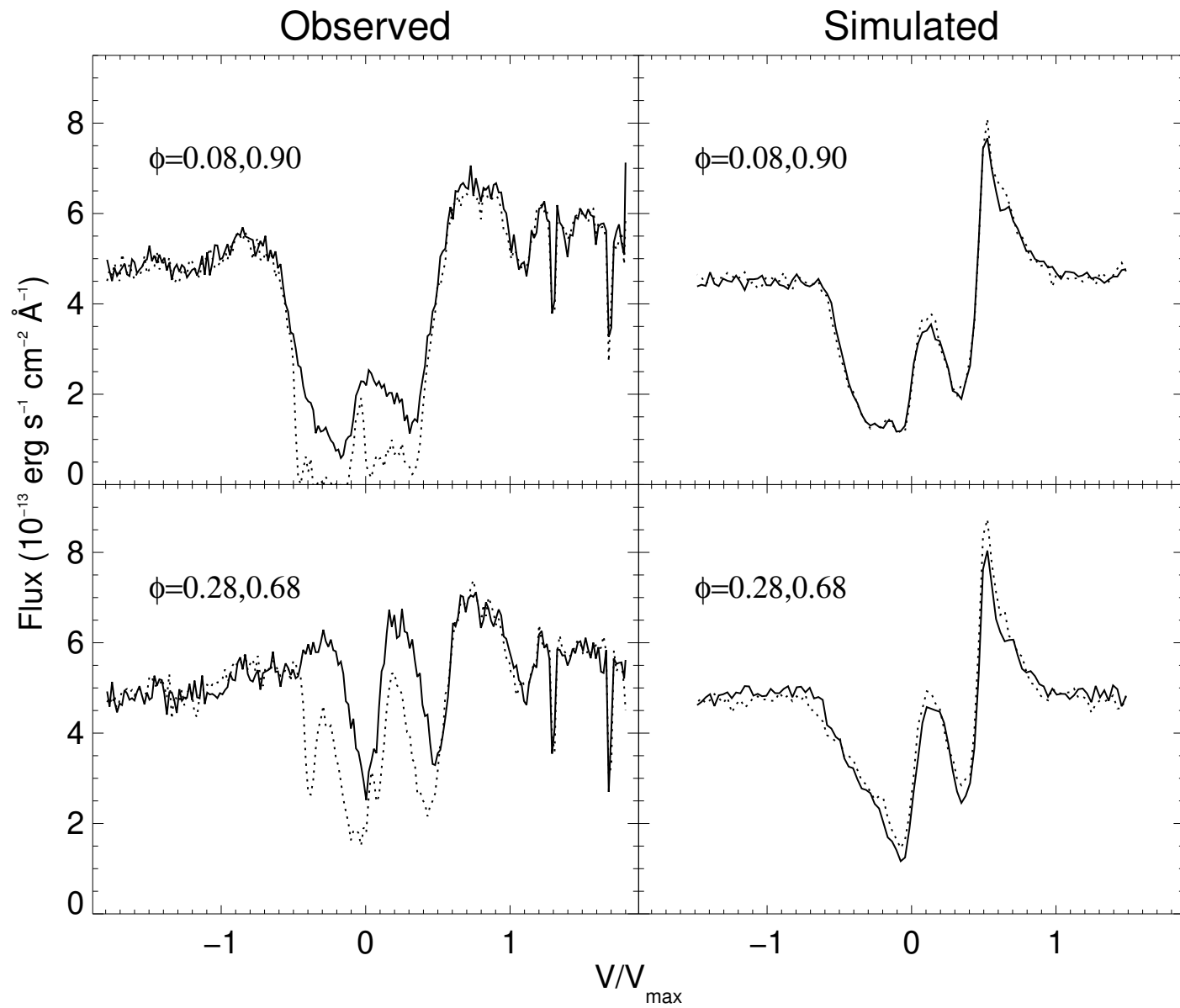


Fig. 8.—

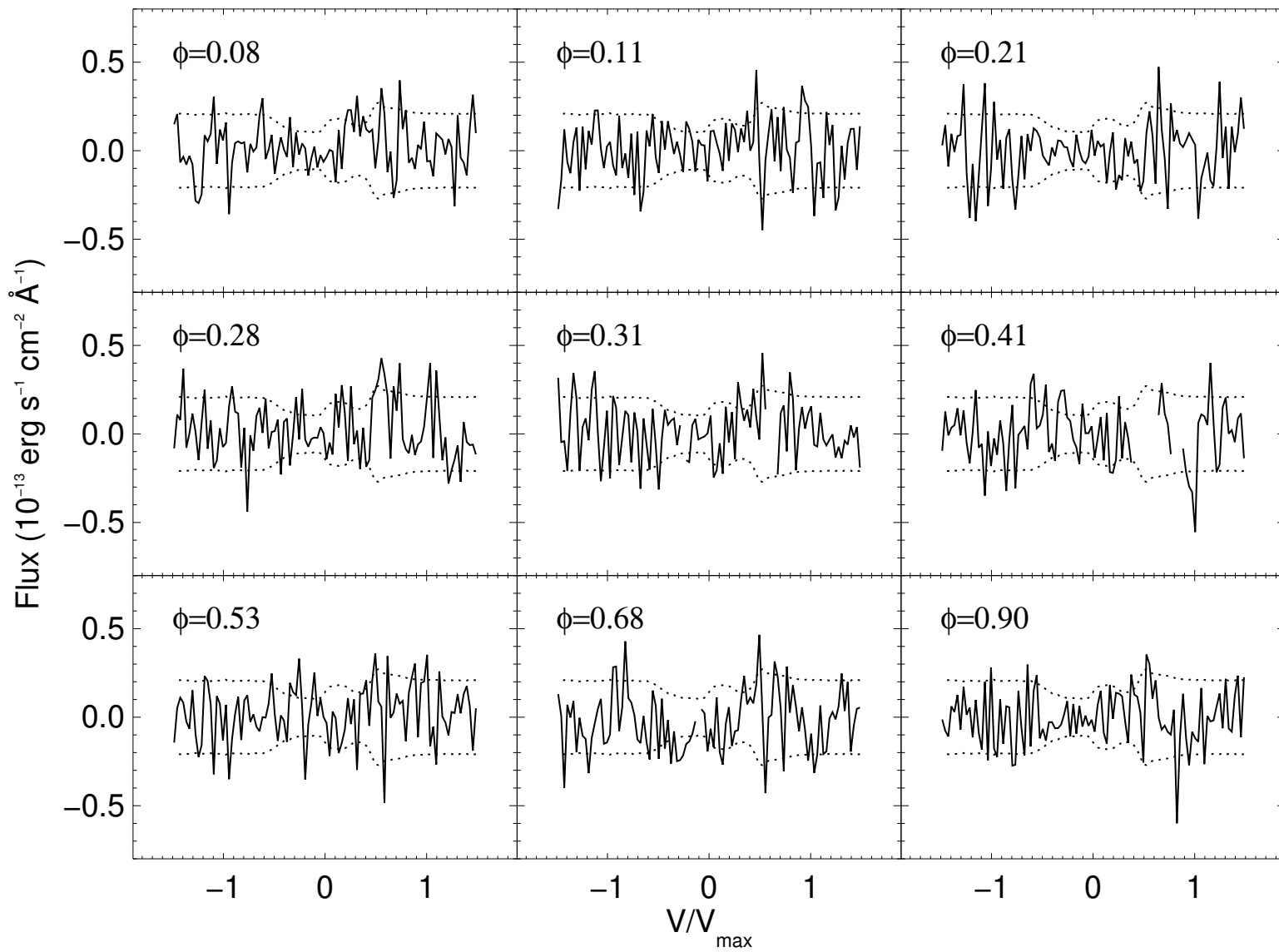


Fig. 9.—

Fig. 10.—

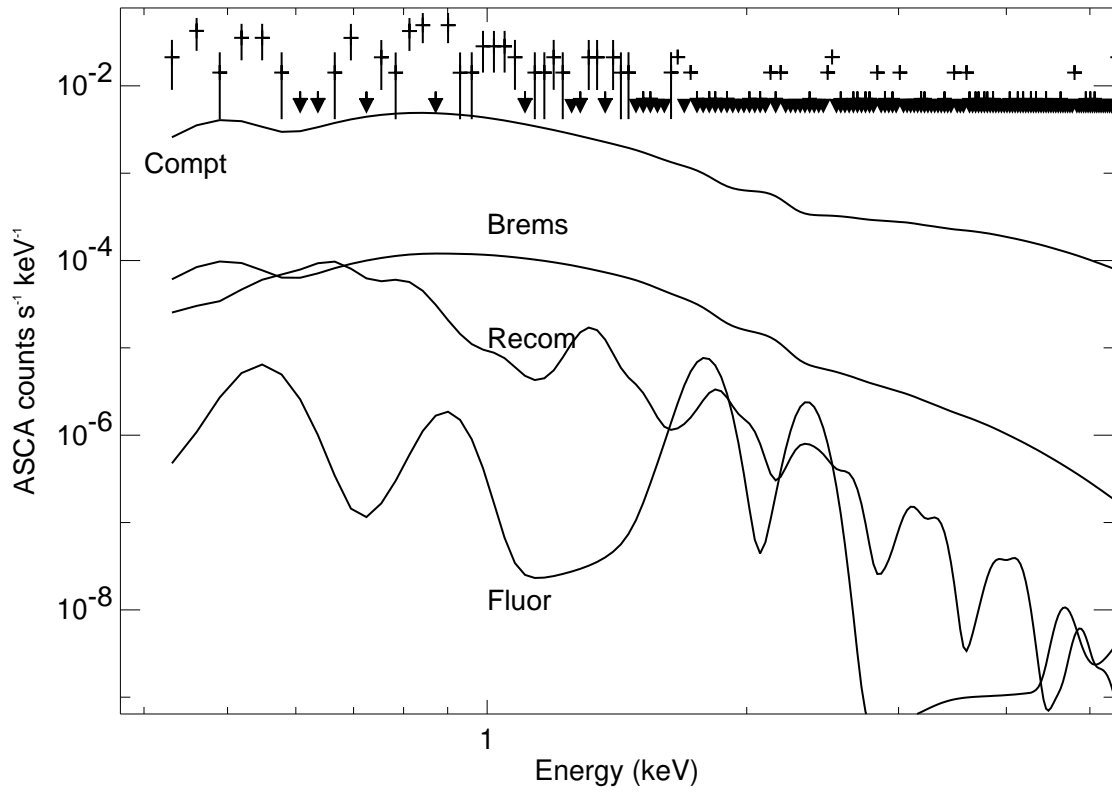
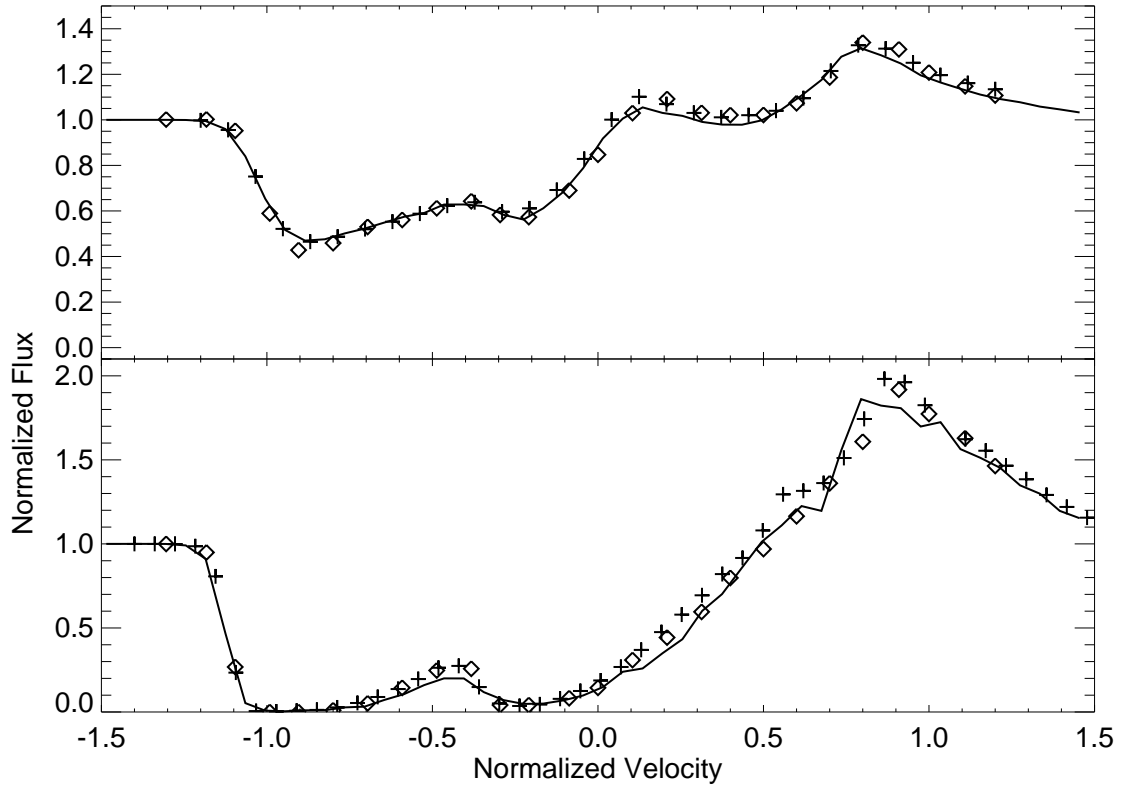


Fig. 11.—



This figure "figure1.jpg" is available in "jpg" format from:

<http://arxiv.org/ps/astro-ph/0012494v1>

This figure "figure2.jpg" is available in "jpg" format from:

<http://arxiv.org/ps/astro-ph/0012494v1>

This figure "figure3.jpg" is available in "jpg" format from:

<http://arxiv.org/ps/astro-ph/0012494v1>

This figure "figure4.jpg" is available in "jpg" format from:

<http://arxiv.org/ps/astro-ph/0012494v1>

This figure "figure5.jpg" is available in "jpg" format from:

<http://arxiv.org/ps/astro-ph/0012494v1>